Rheology of colloidal suspensions in confined flow: Treatment of hydrodynamic interactions in particle-based simulations inspired by dynamical density functional theory

Zahera Jabeen, Hsiu-Yu Yu, David M. Eckmann, Portonovo S. Ayyaswamy, and Ravi Radhakrishnan

Rheology of colloidal suspensions in confined flow: treatment of hydrodynamic interactions in particle-based simulations inspired by dynamical density functional theory

Zahera Jabeen,[1] Hsiu-Yu Yu,[2] David M. Eckmann,[3, 4]

Portonovo S. Ayyaswamy,[1] and Ravi Radhakrishnan[4, 5, *]

[1]*Department of Mechanical Engineering and Applied Mechanics,*

University of Pennsylvania, Philadelphia, Pennsylvania 19104, USA

[2]*Department of Chemical Engineering,*

National Taiwan University, Taipei 10617, Taiwan

[3]*Department of Anesthesiology and Critical Care,*

University of Pennsylvania, Philadelphia, Pennsylvania 19104, USA

[4]*Department of Bioengineering, University of Pennsylvania,*

Philadelphia, Pennsylvania 19104, USA

[5]*Department of Chemical and Biomolecular Engineering,*

University of Pennsylvania, Philadelphia, Pennsylvania 19104, USA

(Dated: September 10, 2018)

Abstract

We investigate the microstructure and rheology of a hardsphere suspension in a Newtonian fluid confined in a cylindrical channel and undergoing pressure-driven flow using Monte Carlo simulations. We develop a hydrodynamic framework inspired by dynamical density functional theory approaches in which the contributions due to various flow-induced hydrodynamic interactions (HI) are included in the form of thermodynamic work done by these HI-derived forces in displacing the hardspheres. Using this framework, we can self-consistently determine the effect of the local microstructure on the average flow-field and vice versa, and co-evolve the inhomogeneous density distribution and the flattening velocity profile with increase in density of suspended particles. Specifically, we explore the effect on the local microstructure due to the inclusion of forces arising from confinement-induced inertial effects, forces due to solvent-mediated interparticle interactions and the dependence of the diffusivity on the local density. We examine the dependence of the apparent viscosity of the suspension on the volume fraction of hardspheres in the cylinder, the flow rate and the diameter of the cylinder, and investigate their effects on the local microstructure.

PACS numbers:

---
*Electronic address: `rradhak@seas.upenn.edu`

I. INTRODUCTION

Rheology of particle-laden suspensions in flow is immensely relevant in the context of widely ranging fields such as the physiology of blood flow [1], slurries in construction industry, petroleum production, manufacturing of cosmetics and pharmaceuticals, in emerging technologies such as 3D printing and micro-fluidics [2], and in geological flows such as molten lava, and hence is a topic of great interest for biotechnology, industrial applications, as well as in disaster management. These colloidal suspensions exhibit complex microstructure when sheared and are characterized by their non-Newtonian behavior, namely, the internal shear stress in these suspensions is a nonlinear function of the applied shear rate. The apparent viscosity of a suspension, $\eta_{\mathrm{app}} = \eta/\eta_0$, defined as ratio of the viscosity of the suspension η to the viscosity of the pure solvent η_0, depends on the suspension microstructure [3, 4], and is determined by properties related to the solutes such as the size, shape, rigidity and its volume fraction, as well as external factors such as the type of flow and the geometry of confinement.

We employ a particle-based approach using Monte Carlo simulations with the inclusion of hydrodynamic interactions inspired by dynamical density functinal approaches to study a suspension of hardspheres in a Newtonian fluid, flowing inside a cylinder. We examine the suspension microstructure and rheological properties as a function of the applied flow rate and the diameter of the cylinder. In previous studies, theoretical approaches have been employed to investigate the dependence of viscosity on the concentration of the solutes. Historically, Einstein [5] in 1911 showed that the apparent viscosity, η_{app} of a suspension of rigid spheres exceeds the viscosity, η_0 of the pure solvent, by a factor proportional to the volume fraction of the spheres ϕ, $\eta_{\mathrm{app}} = \eta_0(1 + \frac{5}{2}\phi)$. This result is valid in the dilute limit $\phi < 0.02$ when the spheres are distant enough such that the disturbance in the fluid elements caused by the first sphere does not affect the other spheres. Batchelor and Green [6] considered the velocity disturbances caused by solvent-mediated pair interactions between the particles, and showed that the apparent viscosity in the semi-dilute limit ($0.02 < \phi < 0.25$) is given by $\eta_{\mathrm{eff}} = \eta_0(1 + 2.5\phi + 7.6\phi^2)$. In denser suspensions, where contact forces dictated by the maximal packing fraction ϕ_m become relevant, Krieger and Dougherty [7] empirically derived the expression $\eta_{\mathrm{eff}} = \eta_0(1 - \phi/\phi_m)^{-B\phi_m}$ in which B and ϕ_m can be used as fitting parameters in experiments. Shear-thinning behavior has also been reported in

experiments at volume fractions $0.25 \leq \phi \lesssim 0.6$ in which the viscosity of the hard-sphere suspensions decreases with increase in shear rate [3, 4]. For volume fractions $\phi \gtrsim 0.6$, a transition to a shear-thickening behavior has been observed [8, 9].

When suspensions are confined between thin slits or in narrow pores, local ordering in the microstructure leads to a change in their macroscopic properties such as isothermal compressibility [10], diffusivity [11] and local viscosity [12]. In addition, when the confined suspensions are subjected to shear flow, the local microstructure exhibits ordering transitions which determine their effective viscosity [13]. The microstructure and rheology of confined suspensions in flow can be studied using direct numerical simulations which involve solving the Navier-Stokes equation such as finite element methods [14], lattice Boltzmann methods [15], or Stokesian dynamics [16]. Even though these methods contain explicit details of the hydrodynamics of the problem, they are limited to small particle numbers, small system size and limited time scales due to the extensive computational costs. In addition, unraveling the complexity of interactions and categorizing them into specific contributions is often not feasible in these methods owing to the multiscale and multiphysics nature of the problem.

An alternative and new approach is to study these systems using field-theoretic approaches such as dynamical density functional theory (DDFT). DDFT [17–20] generalizes the classical density functional theory framework [21] and incorporates the time-dependent effects in the one-body particle density distribution and the corresponding formulation of the free energy functional. A key assumption commonly invoked in DDFT is the "adiabatic approximation" that applies the equilibrium particle correlations to nonequilibrium conditions. Given this assumption, DDFT has been applied vastly to confined colloids in the absence of solvent inertia. For instance, the driven hard sphere dispersions near a confining wall [22] or within a channel [23] were studied through including the non-affine velocity profile arising from the coupling of interparticle interactions with external flow. In the absence of flow but with solvent-mediated pair hydrodynamic interactions included, Brownian diffusion of particles trapped in a time-dependent potential [24, 25] or near a planar wall [20] was investigated. In a 2D channel flow of different-sized particles, the particle distributions and flow rates were characterized with hydrodynamic effects included on a single-particle level [26]. In a similar system of 2D channel flow, the particle-particle pair correlations were determined by fitting the theoretical and experimental particle distributions by making use of the forms of the stress tensor and pair hydrodynamic correlations in the bulk [27]. Beyond

4

the dilute limit, the crowding effects due to local density dependent diffusivity were considered, and the results were compared with Brownian dynamics (BD) simulations [24, 25, 28]. Simultaneous inclusion of solvent-mediated pair hydrodynamic interactions and flow under confinement in DDFT have not been treated in the studies discussed above.

In [29], we studied the microstructure of hardsphere suspensions confined in cylindrical channels at finite temperatures and subject to a pressure-driven flow using dynamical density functional theory. In this theory, starting from the Smoluchowski equation for a system of N particles, we derived a mean-field conservation equation for one-body density distribution by choosing a given representative particle and integrating out the degrees of freedom of the other $N-1$ particles. Employing the adiabatic assumption that correlations active under equilibrium conditions can be applied to nonequilibrium systems, at quasi-steady state, the one-body density was shown to depend on the variation of the excess free energy with respect to the one-body density, the confining potential due to the wall, as well as a work done on the given particle by the lift force as a result of wall-mediated inertial migration. Applying the smoothed-density approximation (SDA) [30] that preserves the hard sphere thermodynamics predicted by the Carnahan-Starling equation of state [31], the excess free energy was feasibly determined. Meanwhile, the average flow field set by the $N-1$ particles was pre-determined approximately based on the experimentally observable blunted profile at the average particle density in the tube.

The quasi-equilibrium density distribution obtained using DDFT was compared with Monte Carlo (MC) simulations as a complementary method to study confined suspensions undergoing flow. We demonstrated that as long as the definitions of the chemical potential of the particle (e.g. the Carnahan-Starling form) and the change of potential energy due to the lift force (the thermodynamic work function) are consistent with DDFT, the two methods lead to equivalent results. In our comparisons, the local particle density was shown to undergo structural ordering due to both inter-particle direct interactions and single-particle wall-mediated inertial migration of the hardspheres given an applied average flow-field. In the dilute limit, we also showed that the results from our DDFT and MC simulations matched with results obtained in experiments in which the hardspheres inside the cylinder were seen to localize in an annulus close to the Segré-Silberberg fixed point $r/R = 2/3$ [32]. However, in this study, the average flow-field, which is known to change due to the presence of hardspheres, was pre-determined and was assumed to be not influenced by the

5

evolving microstructure of the suspension. Moreover, the interparticle interactions between the hardspheres were limited to direct interactions and no pair-hydrodynamic interactions were considered. While the self-diffusivity of the hardspheres was assumed to be modified by the wall confinement, it was considered independent of the local density of the suspension. To address these limitations, it would be appealing to construct a framework that can determine both the particle distribution and the flow profile self-consistently.

In this article, we develop a particle-based MC simulation methodology inspired by the DDFT. By exploiting the equivalence between MC and DDFT, we develop work functions for pair HI and wall-induced HI contributions and obtain the converged density distribution of the hardspheres self-consistently with the evolving flow-field. Our methodology enables us to dissect the various contributions due to HI. The inter-particle or pair-wise HI between the hardspheres contributes to increased layering in the density distribution of the suspended hardspheres, which is further reinforced when we consider the dependence of the diffusivity of the hardspheres on the local density. We then investigate the impact of the local microstructure of the layered suspension on the apparent viscosity of the suspension and explore the change in viscosity with changes in volume fraction, flow velocity and confinement.

The paper is organized as follows. In section II, we discuss the model and give details of the Monte Carlo method. In section III, we present details of the hydrodynamic framework, in which we include the contributions of the various hydrodynamic interactions in the work function and analyze the effect of these HI on the density distribution and the velocity of the suspension. In section IV, we study the dependence of the apparent viscosity of the suspension on the volume fraction of hardspheres, the flow velocity and the diameter of the cylinder. We then conclude with a short section V on future outlook.

II.   MODEL AND THE MONTE CARLO METHOD

A.   Model

Our model consists of a suspension of N neutrally buoyant hardspheres of diameter σ (radius a) in a Newtonian solvent of viscosity η_0 flowing in a cylinder of radius R, length H and volume $V = \pi R^2 H$. The axis of the cylinder is along the x direction. Periodic boundary conditions are imposed in the x-direction, while the walls of the cylinder are assumed to be
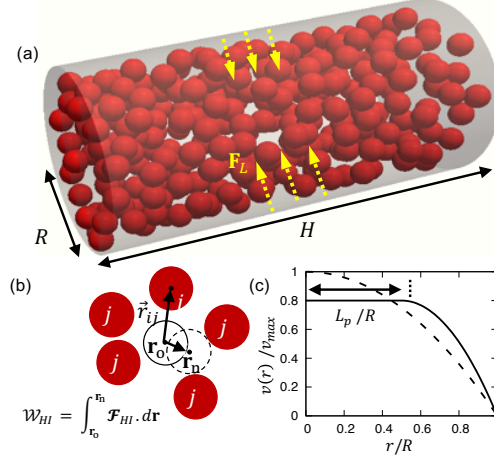
FIG. 1: (a) A collection of hardspheres suspended in Newtonian fluid and confined in a cylindrical channel subjected to a pressure-driven flow. The hardspheres experience an inertial lift force $F^L(r)$ due to the flow (b) A schema of a sphere i experiencing solvent-mediated hydrodynamic interactions (HI) with its neighbors j. The work done by the ith sphere due to displacement from position $\mathbf{r}_0$ to $\mathbf{r}_n$ in the presence of pair HI is given by $\mathcal{W}_{HI}$ (c) The velocity profile $v(r)/v_{max}$ as a function of the radial distance from the axis of the cylinder r. The dashed line represents a Poiseuille flow for dilute suspensions and the solid line represents the blunted velocity profile obtained in the presence of hardspheres. L_P represents the length of the blunted region in the velocity profile.

hard with a no-slip boundary condition, see Fig. 1. The hardspheres cannot overlap with each other, and hence the distance r_{ij} between the centers of two hardspheres i and j is $r_{ij} \geq 2a$. The radial distance of the center of a sphere from the center of the cylinder is given by $r = (y^2 + z^2)^{1/2}$, with $r = 0$ being the position of the axis of the cylinder. Due to the hard interaction of the sphere and the wall, $r \geq R - a$. We also define $h = R - r$ as the distance of the hardsphere from the wall along the radial direction.

The volume fraction of the hardspheres inside the cylinder is defined as $\phi = (\pi/6)\rho\sigma^3$, where $\rho = N/V$. In our simulations, we employ both canonical and grand canonical MC methods. In the case of canonical MC simulations, where the number of hardspheres inside the cylinder N is a constant, we initiate the simulation with an initial number of hardspheres inside the cylinder $N = 1000$. This sets the the length of the cylinder H for a chosen value of R and ϕ. In the case of grand-canonical MC simulations, in which the cylinder is in equilibrium with a reservoir which contains hardspheres with a volume fraction ϕ_R, we initiate the simulation with $N = 400$. In this case, the total chemical potential of the

hardspheres inside the cylinder $\mu = \mu^{id} + \mu^{ex}$ is the same as that of the bulk reservoir $\mu_R(\phi_R)$. Here, $\mu^{id} = k_B T \log \rho \Lambda^3$ is the chemical potential of the ideal gas. The excess chemical potential of the hardspheres inside the bulk reservoir is given by the Carnahan-Starling relation, $\mu_R^{ex}(\phi_R) = \phi_R(8 - 9\phi_R + 3\phi_R^2)/(1 - \phi_R)^3$ [31].

The initial guess for the velocity profile of the flow is taken to be Poiseuille with $v(r) = v_0(1 - r^2/R^2)$, where v_0 is the maximal velocity of the flow observed at $r = 0$. The particle Reynolds number is then given by Re $= a v_0 \rho_0 / \eta_0$ and the Peclet number by Pe $= a v_0 / D_0$. Here, ρ_0 is the density of the solvent, η_0 is the viscosity of the solvent, T is the temperature and D_0 is the Stokes-Einstein diffusivity of the hardsphere in the solvent given by $D_0 = k_B T / 6\pi \eta_0 a$. We assume the temperature to be $T = 300$ K, diameter of the hardsphere to be $\sigma = 2a = 5\mu$m, the velocity of the flow to lie in the range $0 - 5$ cm/sec, and the viscosity η_0 and density ρ_0 of the solvent to be the same as water. Since the diameter of the hardspheres is fixed, a change in the product of the Reynolds number and Peclet number RePe corresponds to a change in the velocity of the flow. We vary our parameters in the range RePe $\in (0, 4000)$, and $R \in (4\sigma, 8\sigma)$. All lengths in the system are scaled by the radius of the hardsphere, i.e. $r \to r/a$. The density of hardspheres at radial position r is expressed in terms of the reduced density $\rho\sigma^3(r)$ [29].

B. Details of the Monte Carlo simulations

We start the simulation with hardspheres randomly distributed in the cylinder. In order to study the flow-induced steady-state distribution of the suspension, we include contributions from the various implicitly active hydrodynamic interactions in the suspension in the form of work functions. These work functions measure the change in energy $\Delta U(\mathbf{r}_i^o \to \mathbf{r}_i^n)$ under the influence of these hydrodynamic interactions when a hardsphere undergoes displacement from position $\mathbf{r}_i^o$ to position $\mathbf{r}_i^n$. The entire simulation is divided into two stages (Fig. 2). In the first stage, we can initiate the suspension inside the cylinder in the canonical or grand canonical ensemble [29, 33] to realize the different conditions (constant N or constant μ) that may prevail in the experiments. The simulation in the second stage is carried out entirely in the canonical ensemble.

In the canonical ensemble, the number of hardspheres N inside the cylinder is held constant and the MC moves consist solely of displacement moves. A random hardsphere

is chosen and displaced from position $\mathbf{r}_i^o$ to $\mathbf{r}_i^n = \mathbf{r}_i^o + [rand]\Delta$, where $[rand]$ is a random number $\in [-1, 1]$, and Δ is the maximum displacement allowed, which is adaptively varied such that only 20% of moves are accepted. If the hardsphere does not overlap with the wall as well as the other hardspheres, the move is accepted with a probability $P_D(\mathbf{r}_i^o \rightarrow \mathbf{r}_i^n)$ defined as

$$P_D(\mathbf{r}_i^o \rightarrow \mathbf{r}_i^n) = \exp[-\frac{1}{k_B T}(\Delta U(\mathbf{r}_i^o \rightarrow \mathbf{r}_i^n))], \tag{1}$$

where, $\Delta U(\mathbf{r}_i^o \rightarrow \mathbf{r}_i^n)$ is the change in energy when the hardsphere is displaced. The change in energy is determined using the work function $\mathcal{W}(\mathbf{r}_i^o \rightarrow \mathbf{r}_i^n) = \int_{\mathbf{r}_i^o}^{\mathbf{r}_i^n} \mathcal{F}(\mathbf{r}').d\mathbf{r}' = -\Delta U(\mathbf{r}_i^o \rightarrow \mathbf{r}_i^n)$, where $\mathcal{F}(\mathbf{r}')$ are the forces due to the relevant hydrodynamics interactions acting on the hardsphere. The details of the work function will be given in the subsequent sections.

In the grand canonical ensemble, the density of spheres inside the cylinder is determined by the chemical potential μ of the hardspheres which is in equilibrium with the chemical potential μ_R of the hardspheres in the reservoir, such that $\mu = \mu_R$. Therefore, in the grand canonical ensemble, in addition to displacement moves, we also include moves in which hardspheres are added and removed with probabilities P_A and P_R respectively. These addition and removal probabilities are defined as:

$$
\begin{aligned}
P_A(N \rightarrow N+1) &= \\
&\frac{V}{\Lambda^3(N+1)} \exp[\frac{1}{k_B T}(\mu^{ex} - U(N+1) + U(N))] \\
P_R(N \rightarrow N-1) &= \\
&\frac{\Lambda^3 N}{V} \exp[-\frac{1}{k_B T}(\mu^{ex} + U(N-1) - U(N))]
\end{aligned}
\tag{2}
$$

Here, $U(N)$ is the potential energy of the N-particle system.

The MC moves in the grand canonical ensemble consist of M_D attempts to displace a particle, M_A attempts to add a hardsphere, and M_R attempts to remove a hardsphere such that the total number of moves $M = M_D + M_A + M_R$, and $M_A/M = M_R/M = 0.15$. Each iteration of either grand canonical or canonical simulations consists of $N \times 10^6$ moves for equilibration and $N \times 10^6$ moves for production and requires 1 CPU-hour for the simulation of a 1500 particle system on a single core of an Intel Xeon 3.5 GHz workstation.

In the following section, we explain the methods used to include contributions from the various hydrodynamic interactions in the thermodynamic work function.
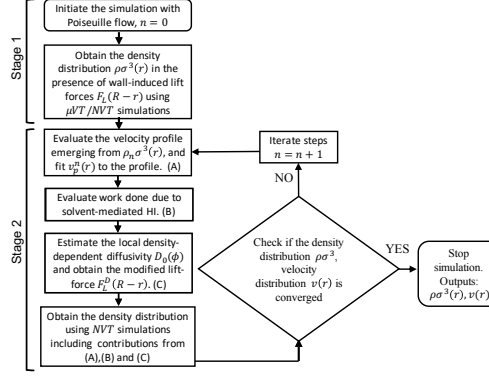
FIG. 2: Implementation of the hydrodynamic framework using MC simulations in two stages is shown by the flowchart.

| | ϕ | | | |
R/σ	RePe = 100	RePe = 200	RePe = 400	RePe = 1000
4	0.068	0.105	0.168	0.290
6	0.059	0.078	0.123	0.228
8	0.057	0.069	0.100	0.187
10	0.056	0.067	0.087	0.162

TABLE I: The volume fraction of the hardspheres ϕ inside the cylinder obtained using grand-canonical MC simulations is given for various radii of the cylinder R and for various RePe.

III.   INCLUSION OF HYDRODYNAMIC INTERACTIONS IN THE THERMODY-NAMIC WORK FUNCTION

In the absence of flow, the only interactions present in the system are the excluded volume effects set up by the hardspheres and the hard wall. This is a well-studied problem in which the hardspheres prefer to adsorb on the wall due to depletion interactions with the wall [34].

When the suspension is subjected to flow, the hardspheres experience hydrodynamic interactions with each other as well as with the wall. In our simulations, we include the hydrodynamic interactions in two stages. A flow-chart of the algorithm is presented in Fig. 2. In the first stage, we equilibrate the microstructure of the suspension by considering only the flow-induced hydrodynamic interaction between the hardspheres and the wall; we label this interaction (O). The implementation of this stage is similar to the method detailed in [29]. The second stage is implemented in the canonical ensemble, where we hold the number

of hardspheres inside the cylinder fixed. In this stage, we include detailed hydrodynamic interactions between the hardspheres in the form of work functions.

A summary of the essential features of our approach is provided here. Detailed methodological aspects are discussed separately in later sections. (A) The presence of hardspheres in the fluid changes the viscosity of the suspension locally, thereby affecting the velocity and density distribution of the hardspheres. We estimate this collective effect using an iterative calculation where the velocity distribution and density distribution obtained are self-consistent. (B) In the fluid medium, the trajectories of the hardspheres are driven by solvent-mediated long-range interactions with other hardspheres. These interactions result in an altered non-local mobility tensor for each hardsphere which couples the displacement of a hardsphere with the positions of the rest of the hardspheres. We include a first-order approximation of the inter-particle hydrodynamic interactions by estimating the work done in displacing a hardsphere in the presence of solvent-mediated interactions with its nearest neighbors. (C) The short-time diffusion coefficients of the hardspheres depend on the density of hardspheres in the neighborhood, with the diffusivity showing a decrease with increase in density. We include density-dependent diffusivity in our calculations to account for this effect.

In the following sections, we explain the method of including interactions {(O),(A),(B),(C)} as well as discuss the implications of including these interactions for the microstructure and rheology of the suspension.

A. Inclusion of wall-induced hydrodynamic interactions

In the first stage (Fig. 2), we assume that in the presence of flow, the hydrodynamic interactions active in the suspensions are limited to the wall-induced lift-force $F^L(r)$ acting on the hardspheres, as detailed in our earlier paper [29]. We adopt the approximation derived by Cox-Hsu for the inertial migration velocity $v_M(r)$ for a hardsphere near a plane wall flowing at a radial distance r from the axis of the cylinder in parabolic flow [35]. The inertial lift-force $F^L(r)$ acting on the particle can be determined from the migration velocity $v_M(r)$ as:

$$\frac{F^L(r)}{k_{\mathrm{B}}T} = \frac{v_M(r)}{D_\perp},$$ (3)

which yields the following expression for the inertial lift-force $F^L(r)$ directed along the radial direction r:

$$\frac{F^L(r)}{k_B T} = -\text{RePe}\frac{D_0}{D_\perp}\frac{5}{288}\left(\frac{a}{L^2}\right)\left(1 - (\frac{R-r}{L})\right)\left(22 - 73(\frac{R-r}{L})\right). \tag{4}$$

Here, $D_\perp$ is the altered normal diffusivity of a hardsphere in the presence of a wall and has been derived by Bevan-Prieve [36] as $D_\perp = D_0/\beta_\perp$, where $\beta_\perp = \frac{6(z-1)^2+9(z-1)+2}{6(z-1)^2+2(z-1)}$ with $z = (R-r)/a$. The expression for the lift force given by Cox-Hsu has a fixed point at $r_C/R = 51/73 = 0.698$, which is close to the Segré -Silberberg fixed point at $r/R = 2/3$ [32].

The change in energy when a hardsphere undergoes radial displacement from radial position r_o to r_n under the influence of the inertial lift force $F^L(r)$ is given by $\Delta U^L(r_o \to r_n) = -\int_{r_o}^{r_n} F^L(r).dr$. We can then define the total N-particle potential energy of the system as $U^L(N) = \sum_{i=1}^N U^L(r)$, where the single particle potential energy of the hardsphere is given by $U^L(r) = \int_r^{L_p} F^L(r').dr'$, since the lift-force vanishes at $r = L_p$, where the shear-rate is zero.

In this stage of the simulations, we can obtain the equilibrated microstructure of the suspension in either the canonical or grand canonical ensemble. In the grand canonical ensemble, since the effective chemical potential $\mu_{\text{eff}}(r)$ inside the cylinder is determined by the excess chemical potential μ^{ex} as well as the N-particle potential energy $U(N)$ which depends on the product RePe (see eq. 2), the volume fraction of hardspheres ϕ inside the cylinder registers an increase with increase in the product RePe (see Table I).

We showed in [29] that the variations in the reduced density of the hardspheres $\rho\sigma^3(r)$ obtained in the radial direction r is indicative of the inertial migration of the hardspheres in the presence of flow. In the presence of flow, the density near the wall as well as near the axis of the cylinder decreases, whereas a peak develops in the density distribution close to r_C at high RePe. The reduced density $\rho\sigma^3$ obtained in the grand canonical ensemble for a reservoir volume fraction $\phi_R = 0.05$ and RePe= 400 is shown by dashed line in Fig. 3(b). The peak of the reduced density distribution is seen at $r_p/R = 0.8$ as compared to $r_p/R = 0.875$ for RePe= 0.

In the case of dilute suspensions, the velocity profile of the suspension is a Poiseuille. However, when the volume fraction inside the cylinder is significant enough for hardspheres to interact with each other, the Poiseuille profile may be irrelevant. In the following section,

we describe the second stage of the simulations, in which simulations are carried out in the canonical ensemble. We start with the discussion of a self-consistent method that resolves the disparity between the input velocity profile and the velocity profile that results from the spatially dependent density of hardspheres in the suspension.
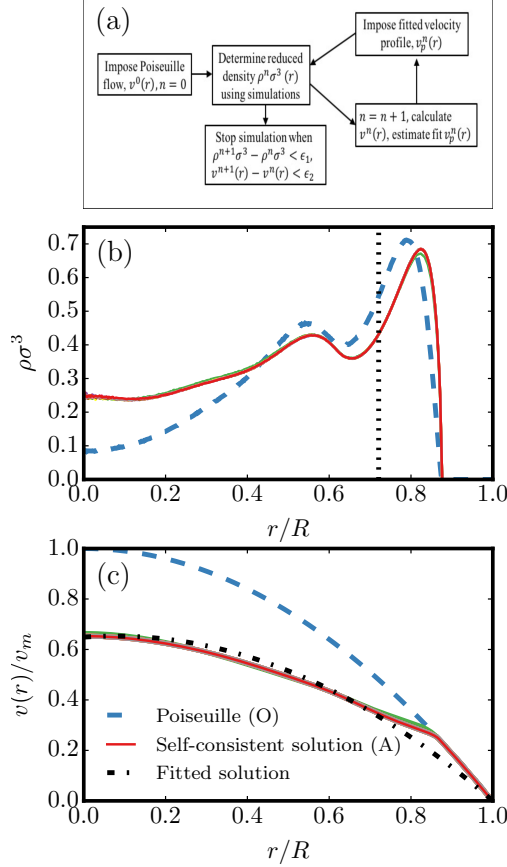

FIG. 3: (a) Method to obtain the self-consistent velocity and density distribution is shown by the flowchart (b) Reduced density distributions at different scaled radial positions r/R obtained for RePe= 400, $\phi_R = 0.05$ when the incident velocity profile is Poiseuille flow (dashed line) and when the incident velocity profile is blunted (solid lines). In the latter case, in addition to the converged density distribution, five intermediate iterations at equally spaced intervals are also plotted. (c) Velocity profile in the radial direction is plotted. Dashed line represents Poiseuille flow, solid lines show the velocity profiles obtained from density-dependent Ho-Leal calculation, and dashed-dot line represents the optimum fit to the velocity profile. Here $L_p/R = 0.075$.

13

B. Self-consistent calculation of the velocity profile and the density distribution

Experiments have shown that the presence of spheres in suspension changes the velocity distribution from a pure Poiseuille flow to a blunted flow profile [37, 38]. These studies demonstrated that the change in the velocity profile of the suspension with increase in the density of hardspheres is two-fold: (a) the velocity at the center decreases with increase in density, and (b) the flatness of the velocity profile increases. Ho and Leal presented a method to estimate the velocity of a dilute suspension exhibiting a non-uniform density distribution at steady state [39]. Their formalism is based on the premise that a non-uniform density distribution leads to a spatially varying viscosity. Travis et al also discussed the existence of a spatially varying and and potentially non-local viscosity due to local variations in pressure tensors which are functions of the local density [40]. We extend the Ho-Leal formalism to semi-dilute suspensions such as obtained in our simulations and implement an iterative scheme for the self-consistent calculations of the velocity profile and density distribution (Fig. 3(a)). As depicted in Fig. 3(b) (dashed line), the reduced density distribution in the presence of wall-induced inertial forces shows regions of high and low density in the radial direction. This gives rise to strong spatial variations in the local viscosity in the radial direction. In the bulk, such a variation in local viscosity can be approximated using the Batchelor-Green expression [6], which relates the apparent viscosity of a suspension of hardspheres to the bulk volume fraction ϕ. Assuming that a similar relation can be employed in the confined suspension, in which the local viscosity in the radial direction is related to the local volume fraction, we obtain $\eta(r) = \eta_0(1 + 2.5\phi(r) + 7.6\phi^2(r))$; this amounts to a local density approximation. Here, the local volume fraction is related to the local reduced density as $\phi(r) = \frac{\pi}{6}\rho\sigma^3(r)$. The Stokes' equation can then be written as:

$$\frac{1}{r}\frac{\partial}{\partial r}\left(r\eta(r)\frac{\partial v(r)}{\partial r}\right) = -\frac{\Delta P}{L}. \tag{5}$$

Solving for the velocity of the suspension and employing the boundary conditions $dv/dr = 0$ at $r = 0$, and $v(r) = 0$ at $r = R$, we obtain:

$$v(r) = \frac{\Delta P}{2L\eta_0}\int_r^R \frac{r'dr'}{1 + 2.5\phi(r') + 7.6\phi^2(r')}. \tag{6}$$

This expression for velocity $v(r)$ includes the collective hydrodynamic contribution of the presence of hardspheres in the suspension, and reduces to the expression for Poiseuille flow,

14

in the absence of any hardspheres in the suspension (i.e. when the local volume fraction $\phi(r) = 0$). In Fig. 3(c), the reduced velocity profile $v(r)/v_0$ obtained for the density distribution shown by dashed line is plotted as a function of radial position by solid line in Fig. 3(b). Here, $v_0 = \frac{\Delta P R^2}{4 L \eta_0}$. We see that the velocity profile significantly deviates from the Poiseuille flow profile shown by dashed line. Specifically, the ratio of maximum velocity obtained at $r = 0$ to the applied centerline velocity $v_m/v_0 < 1$. Near $r = 0$, the velocity profile appears blunted, indicating a nearly zero shear stress in this region.

We fit the following expression to the velocity profile, in which the velocity in the blunted region is approximated by a flat velocity v_m, and the rest of the velocity profile is fitted to a shifted Poiseuille flow (also see Fig. 1(c)):

$$
\begin{aligned}
v_p(r) &= v_m, & \text{for } 0 < r < L_p, \\
& v_m\left(1 - \left(\tfrac{r - L_p}{R - L_p}\right)^2\right) & \text{for } L_p < r < R.
\end{aligned}
\tag{7}
$$

The length of the blunt region L_p in the fitted velocity profile $v_p(r)$ is estimated by minimizing the squared sum $\Sigma = (v(r) - v_p(r))^2$. We then impose this fitted velocity profile on the suspension as driving the flow in the canonical ensemble. In the blunt region, the particles do not experience a lift force, whereas the particles experience a lift force given by the Cox-Hsu expression (eq. 4) in the parabolic region, the length of the parabolic region being $L = R - L_p$. Let us denote the calculated velocity profile, fitted velocity profile and the reduced density by the iteration index n, i.e. $v^n(r)$, $v_p^n(r)$ and $\rho^n \sigma^3(r)$ respectively. We recalculate the velocity profile $v^{n+1}(r)$ using the density $\rho^n \sigma^3(r)$, and impose the fitted velocity profile $v_p^{n+1}(r)$ to estimate the density distribution $\rho^{n+1} \sigma^3(r)$, until a convergence in the velocity profile and the density is obtained such $v^{n+1}(r) - v^n(r) < v_0 \epsilon_1$, and $\rho^{n+1} \sigma^3(r) - \rho^n \sigma^3(r) < \epsilon_2$; for numerical convergence, we choose $\epsilon_1 = \epsilon_2 = 0.001$. We denote the converged reduced density $\rho \sigma^3(r)$ and the velocity distribution $v(r)$ without indices, see Fig. 3(a).

In Fig. 3(b) and (c), we plot five intermediate iterates as well as the converged results of the reduced density $\rho^n \sigma^3(r)$ and the velocity distribution $v^n(r)$. We note that convergence is attained typically within the first ten iterations. The local density of hardspheres changes under the influence of the self-consistently obtained velocity profile. First, we see that the density in the center of the cylinder $\rho \sigma^3(r)$ shows an increase when the self-consistent velocity profile is applied as compared to the Poiseuille profile. The higher density in the center can be attributed to the zero lift force felt by the hardspheres in the blunted region of the velocity profile. Second, the peak of the reduced density shown by solid line shows

15

a displacement to the right towards the wall in comparison to the density shown by dashed line. The origin of this displacement can be explained by the shifted parabolic form of the velocity profile given by eq. 7 which has a fixed point closer to the wall.

Hence, using the iterative self-consistent calculation demonstrated in this section, we show that the average velocity profile of the suspension is modified in the presence of hardspheres in the suspension. The suspension flows with a slower velocity than the incident velocity profile incurring a loss in energy due to viscous dissipation in the fluid. The nature of the velocity profile in turn affects the microstructure of the suspension, with more hardspheres flowing closer to the wall for blunted velocity fields in comparison to a Poiseuille velocity field. Next, we demonstrate a method to include solvent-mediated pair hydrodynamic interactions in our calculation.

C. Inclusion of solvent-mediated pair hydrodynamic interactions

In semi-dilute colloidal suspensions, a significant interaction that needs to be considered is the hydrodynamic interactions (HI) between the hardspheres mediated by the disturbances in the surrounding solvent. This interaction arises when a hardsphere moves due to the flow and disturbs the fluid around it. These disturbances are long-range and influence the motion of the other hardspheres and are represented in the form of a mobility tensor $\boldsymbol{M}_{ij}$ which couples the perturbations in velocity of a given sphere i due to the displacement-inducing forces F_j acting on the rest of the spheres j, such that the change in the velocity of the ith hardsphere is given by:

$$\delta \boldsymbol{v}_i = \sum_j \boldsymbol{M}_{ij}.\boldsymbol{F}_j \tag{8}$$

The mobility tensor $\boldsymbol{M}_{ij}$ depends on the geometrical dimensions of the spheres [41] and the confinement [42]. In addition to far-field hydrodynamic interactions, lubrication effects become increasingly significant when the hardspheres are either close to the wall or when they flow in close proximity to each other such as in dense suspensions. The collective effect is captured in Stokesian dynamics [43], in which an inverse mobility tensor can be estimated which captures both far-field interactions as well as lubrication interactions. However, because this method involves inverting a $3N \times 3N$ matrix at every time step, there is a limitation on the number of hardspheres which can be investigated. A simplification in the case of semi-dilute suspensions in the bulk is to consider the Rotne-Prager-Yamakawa tensor (RPY)

[44, 45] which gives a positive-definite approximation for far-field hydrodynamic interactions between two equal-sized spheres in bulk solution in terms of the instantaneous inter-particle distances r_{ij} between the hardspheres. We adopt this form in the current work. In the case of a suspension of non-overlapping hardspheres ($r_{ij} \geq \sigma$), the mobility tensor can be written as:

$$
\boldsymbol{M}_{ij} = \begin{cases} M_0 \boldsymbol{I}, & i = j \\ \frac{1}{8\pi\eta_0 r_{ij}} \left[(1 + \frac{2a^2}{3r_{ij}^2})\boldsymbol{I} + (1 - \frac{2a^2}{r_{ij}^2})\frac{\mathbf{r_{ij}r_{ij}}}{r_{ij}^2} \right], & i \neq j \end{cases} \tag{9}
$$

Here, $\boldsymbol{r}_{ij} = \boldsymbol{r}_i - \boldsymbol{r}_j$ is the vector joining the positions of the spheres i and j. Let us define $x_{ij} = x_i - x_j$, $y_{ij} = y_i - y_j$, $z_{ij} = z_i - z_j$ such that the distance between the two spheres is given by $r_{ij} = |\boldsymbol{r}_{ij}|$. For simplicity, we introduce new notations for the following terms in eq. 9:

$$
\alpha(r_{ij}) = \frac{6a}{8r_{ij}}(1 + \frac{2a^2}{3r_{ij}^2}), \gamma(r_{ij}) = \frac{6a}{8r_{ij}}(1 - \frac{2a^2}{r_{ij}^2}).
$$

It is evident from eq. 9 that the leading-order contribution of the solvent-mediated hydrodynamic interactions decays as $1/r$. In the vicinity of a wall, corrections arising from contributions of the mirror images of the disturbances need to be included as is done in the Rotne-Prager-Blake mobility tensor[46], where the leading-order contribution to the hydrodynamic interactions decays as $1/r^2$, and hence are shorter-ranged compared with eq. 9. In this study, in order to account for the effects due to solvent-mediated pair hydrodynamic interactions in addition to the immediate wall-induced lift force, we adopt the form of the RPY tensor to include the pair HI among the nearest neighbors while including the wall effects on the self mobility of the hardsphere M_0. We delineate our efforts in the following paragraph.

In the case of a bulk suspension, the diagonal elements of the mobility tensor $\boldsymbol{M}_{ij}$ (eq. 9) constitute the self-mobility of the hardspheres, which is given by the Stoke's coefficient $M_0 = \boldsymbol{M}_{ii} = (1/6\pi\eta_0 a) = D_0/k_\mathrm{B}T$. In the presence of confinement, the symmetry in the self-mobility term is broken, and the diagonal elements consist of terms $\boldsymbol{M}_{ii} = (M_{x,i}, M_{y,i}, M_{z,i})$ which can further be resolved into components parallel and perpendicular to the confinement, which are called the drag mobility ($M_\parallel$) and the normal mobility ($M_\perp = M_r$) respectively. Closed form expressions for the drag mobility and the normal mobility of a sphere at a distance h from a plane surface have been given by Bevan and Prieve [36]. Expanding eq. 8

17

and eq. 9, we obtain:

$$
\begin{aligned}
\delta v_{x,i} = M_{x,i}F_{x,i}+ \ & D_{x,i}\sum_j[(\alpha(r_{ij})+\gamma(r_{ij})x_{ij}x_{ij})\frac{F_{x,j}}{k_{\mathrm{B}}T} \\
& +\gamma(r_{ij})x_{ij}y_{ij}\frac{F_{y,j}}{k_{\mathrm{B}}T}+\gamma(r_{ij})x_{ij}z_{ij}\frac{F_{z,j}}{k_{\mathrm{B}}T}], \\
\delta v_{y,i} = M_{y,i}F_{y,i}+ \ & D_{y,i}\sum_j[(\alpha(r_{ij})+\gamma(r_{ij})y_{ij}y_{ij})\frac{F_{y,j}}{k_{\mathrm{B}}T} \\
& +\gamma(r_{ij})y_{ij}x_{ij}\frac{F_{x,j}}{k_{\mathrm{B}}T}+\gamma(r_{ij})y_{ij}z_{ij}\frac{F_{z,j}}{k_{\mathrm{B}}T}], \\
\delta v_{z,i} = M_{z,i}F_{z,i}+ \ & D_{z,i}\sum_j[(\alpha(r_{ij})+\gamma(r_{ij})z_{ij}z_{ij})\frac{F_{z,j}}{k_{\mathrm{B}}T} \\
& +\gamma(r_{ij})z_{ij}x_{ij}\frac{F_{x,j}}{k_{\mathrm{B}}T}+\gamma(r_{ij})z_{ij}y_{ij}\frac{F_{y,j}}{k_{\mathrm{B}}T}],
\end{aligned}
\tag{10}
$$

In our system of interest, the force driving the displacement of the hardsphere along the x-direction consists of the drag force, and the corresponding force along the radial direction consists of the radial inertial lift force $F^L(r)$. The driving forces along the y and z axis then are the components of the radial lift force $F^L(r)$ along the y and z direction. Under quasi-equilibrium conditions, the velocity disturbances in x-direction do not alter the radial distribution of particles in the mean-field limit. Therefore, when constructing the work function for displacing the particle, we only consider velocity disturbances due to solvent-mediated hydrodynamic interactions in the y and z directions. Since, the velocity of the flow along the radial direction is zero, the velocity disturbances of the hardspheres can be reduced to the velocity of the hardspheres in the y and z direction respectively, i.e. $\delta v_{y,i}=v_{y,i},\delta v_{z,i}=v_{z,i}$. The velocity of the hardspheres in the y and z directions are then given by:

$$
\begin{aligned}
v_{y,i} = M_{y,i}F_{y,i}+ \ & D_{y,i}\sum_j[(\alpha(r_{ij})+\gamma(r_{ij})y_{ij}y_{ij})\frac{F_{y,j}}{k_{\mathrm{B}}T} \\
& +\gamma(r_{ij})y_{ij}z_{ij}\tfrac{F_{z,j}}{k_{\mathrm{B}}T}], \\
v_{z,i} = M_{z,i}F_{z,i}+ \ & D_{z,i}\sum_j[(\alpha(r_{ij})+\gamma(r_{ij})z_{ij}z_{ij})\frac{F_{z,j}}{k_{\mathrm{B}}T} \\
& +\gamma(r_{ij})z_{ij}y_{ij}\tfrac{F_{y,j}}{k_{\mathrm{B}}T}].
\end{aligned}
\tag{11}
$$

We note that the first terms on the right hand side of eq. 11 represent the components of the wall-induced lift forces along the y and z directions which are similar to the forces considered in [29]. Importantly, the second terms on the r.h.s. represent the corrections due to the solvent-mediated pair hydrodynamic interactions. We can obtain the velocities in the

radial and azimuthal directions $(v_i(r), v_i(\theta))$ by transforming the velocities $(v_{y,i}, v_{z,i})$:

$$\begin{pmatrix} v_i(r) \\ v_i(\theta) \end{pmatrix} = \begin{pmatrix} \cos\theta & \sin\theta \\ -\sin\theta & \cos\theta \end{pmatrix} \begin{pmatrix} v_{y,i} \\ v_{z,i} \end{pmatrix}, \tag{12}$$

where, the angle $\tan\theta = z/y$. The total force $\mathcal{F}_i(r)$ experienced by the ith hardsphere at radial position r can then be inferred from the relation:

$$\mathcal{F}_i(r) = \frac{v_i(r)}{M_{\perp,i}}, \tag{13}$$

where, the normal mobility of the hardsphere is related to the radial diffusion coefficient $D_{\perp,i}$ by the relation $M_{\perp,i} = D_{\perp,i}/k_{\mathrm{B}}T$. Here,

$$\mathcal{F}_i(r) = F_i^L(r) + F_i^{HI}(r), \tag{14}$$

where, the first term on the right hand side $F_i^L(r)$ represents the contribution from the inertial lift force in the radial direction (eq. 3), while the second term $F_i^{HI}(r)$ represents the additional contribution to the radial forces acting on the hardspheres due to solvent-mediated hydrodynamic interactions between the hardspheres. To obtain a first-order contribution to the radial forces acting on the hardspheres due to solvent-mediated HI, we now limit the solvent-mediated HI to the nearest neighbors. We estimate this region of nearest neighbor interaction by calculating the position of the first minimum of the in-plane radial distribution function calculated for hardspheres belonging to the same peak, which was found at a distance 1.3σ. Hence, we limit the region of interaction to a sphere of radius $r_c^{HI} = 1.3\sigma$ (see Fig. 1(b)) such that solvent-mediated hydrodynamic interactions between hardspheres with centers belonging to this sphere are alone counted.

We can then construct a work function by determining the work done by the particle i in moving from the radial position r_i^o to r_i^n. The contribution to the work function due to solvent-mediated hydrodynamic interactions is then given as:

$$\mathcal{W}^{HI}(r_i^o \to r_i^n)/k_{\mathrm{B}}T = \int_{r_i^o}^{r_i^n} F_i^{HI}(r)dr. \tag{15}$$

The change in energy when the particle is displaced in the presence of solvent-mediated hydrodynamic interactions is given by $\Delta U^{HI}(r_i^o \to r_i^n) = -\mathcal{W}^{HI}(r_i^o \to r_i^n)$ such that the net change in energy when a particle is displaced is given by:

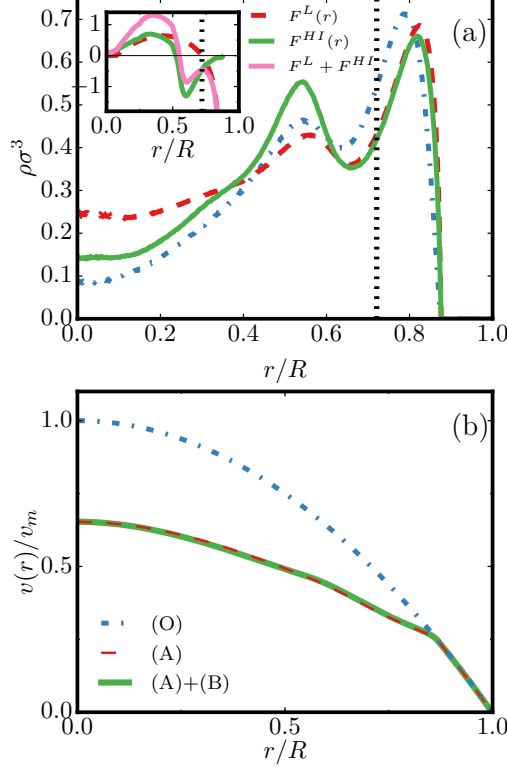$$\Delta U(\mathbf{r}_i^o \to \mathbf{r}_i^n) = \Delta U^L(r_i^o \to r_i^n) + \Delta U^{HI}(r_i^o \to r_i^n). \tag{16}$$

FIG. 4: (a) Reduced density distribution $\rho\sigma^3$ obtained for RePe= 400 when the solvent-mediated pair-HI between particles is included in the presence of average velocity profile obtained using self-consistent calculation (solid-line, (A)+(B)). Also shown are density distribution obtained when the incident flow is Poiseuille (dashed-dot line, (O)) and when the incident flow is corrected using self-consistent calculation (dashed line, (A)). Pair-HI enhances collective migration of the particles leading to depletion in the center, and formation of an additional peak. Inset shows the forces due to the lift $F^L(r)$ and pair-HI $F^{HI}(r)$, and their sum $F^L + F^{HI}$ plotted as a function of the scaled radial distance from the center r/R. (b) Velocity distribution plotted for various hydrodynamic interactions included. Legends for plots (a) and (b) are common.

In our MC simulations, the energy change in eq. 16 is factored into the acceptance probability for particle displacements.

In Fig. 4(a), the reduced density obtained along the radial direction with various hydrodynamic interactions included are shown. The solid line represents the density obtained when the hardspheres experience solvent-mediated pair interactions (B) in addition to the wall-induced lift-forces in the presence of the blunt-parabolic velocity distribution obtained using self-consistent calculation (A). Dashed line represents the reduced density obtained

when only interactions (A) are considered and dashed-dotted line indicates the reduced density obtained when wall-induced lift forces in the presence of incoming Poiseuille flow are considered (O). In the reduced density obtained when interactions (A)+(B) are included, the primary peak observed near the wall is seen to shift away from the wall and towards r_C. In addition, an enhanced secondary peak is observed next to the primary peak indicating an increased layering of the hardspheres in the suspension. Formation of the two peaks in the density is accompanied by a depletion in the the density in the center of the cylinder. We note that the collective migration of the hardspheres due to the solvent-mediated hydrodynamic interactions between the neighboring hardspheres drives the depletion of hardspheres in the center as well as their accumulation in the two peaks.

Further evidence of the collective migration of hardspheres can be gleaned from the inset to Fig. 4(b), in which the average radial force due to hydrodynamic interactions $F^{HI}(r)$ and due to individual lift force $F^L(r)$ acting on a hardsphere at a radial position r are plotted as a function of the radial distance from the center r. We reiterate here that the form of the lift-force $F^L(r)$ is given by the Cox-Hsu velocity profile (eq. 4) and is determined by the confinement as well as the details of the velocity profile. The average force due to solvent-mediated HI, $F^{HI}(r)$ however is decided by the local microstructure of the suspension in addition to the effective lift-forces acting on the hardsphere. We observe that the region in which the wall-induced lift-force $F^L(r)$ tends to displace the hardsphere away from the wall ($F^L(r) < 0$) lies in the interval $r_C/R \leq r/R < (R-a)/R$. The force due to solvent-mediated HI $F^{HI}(r)$ for the same value of the product RePe however tends to displace the hardspheres away from the wall and towards the center in the region $0.52 \leq r/R < (R-a)/R$. Hence, the region in which the hardspheres experience a force directed away from the wall is greater when the solvent-mediated HI is included. This can be attributed to the collective migration of the hardspheres due to the nearest neighbor solvent-mediated HI between the hardspheres. The contributions of the hardspheres lying in the region $r > r_C$ to the solvent-mediated HI force $F^{HI}(r)$ acting on the hardspheres within its radial proximity is radially directed towards the center. These contributions from the nearest neighbors dominate due to the higher density fo hardspheres in the primary peak, and result in a net force $F^{HI}(r)$ which is negative and drives the hardspheres collectively away from the wall and towards the center. Such collective migration of colloids in the presence of solvent-mediated HI has been observed in confined colloids [47]. Next, we plot the effective radial force acting on the

21

hardspheres $\mathcal{F}(r) = F^L(r) + F^{HI}(r)$ in the inset to Fig. 4(a) which shows a fixed point widely different from r_C, which is much closer to the central axis of the cylinder in comparison to r_C. Meanwhile, the effective radial force $\mathcal{F}(r)$ near the central region is larger in comparison to the wall-induced lift force. This implies that a larger number of particles migrate away from the center towards the fixed point near $r^\star \sim 0.53$ resulting in the formation of a secondary but significant peak in the density distribution of hardspheres.

Finally, we plot the velocity profile corresponding to this reduced density in Fig. 4(b). We can observe slight oscillations in the velocity profile which develop due to the layering of the hardspheres in the radial direction of the cylinder. We note that the contributions to the free energy functional due to the pair interactions increase with increase in RePe, and more substantial changes are seen in the velocity distribution at higher RePe. Next, we study the effect of including density-dependent diffusivity on the microstructure of the suspension.

D. Inclusion of density-dependent diffusion coefficients

In the previous sections, we observed that the density of hardspheres along the radial direction of the cylinder is not uniform with regions of high density of hardspheres seen at the peaks and regions of low density in the center. The inhomogeneity in density is expected to lead to an inhomogeneity in the instantaneous diffusion of the hardspheres. In bulk suspensions, the dependence of the short-time and long-time diffusion coefficients on the volume fraction ϕ of the suspension has been studied both theoretically [48–50] and experimentally [51], in which it was observed that the diffusion coefficient decreases with an increase in the volume fraction of the suspension. This was determined to be mainly a hydrodynamic effect in which correlations arising from both short-range and long-range hydrodynamic interactions contribute to the short-time diffusion coefficients, and overshadow the contributions due to direct interactions between the hard-spheres [49]. However in confined fluids, the diffusion coefficient is further modified by the local microstructure and the effects of confinement [52, 53] to result in a density-dependent diffusion coefficient in the radial direction. In this study, in order to capture such effects due to the cylindrical wall and the local microstructure, we define a radial diffusion-coefficient which depends on the local volume fraction $\phi(r)$ as:

$$D_\perp(\phi(r)) = D_0(\phi(r))/\beta_\perp(r). \tag{17}$$

22

Here, $\beta_\perp(r)$ is the correction due to confinement proposed by Bevan and Prieve [36]. The density dependence of the diffusion coefficient $D_0(\phi(r))$ is determined using the expression derived in [49], given by:

$$D_0(\phi(r)) = D_0/[1 + L(\phi(r))], \tag{18}$$

where,

$$
\begin{aligned}
L(\phi(r)) &= \frac{2b^2}{1-b} - \frac{c}{1+2c} + [\frac{2bc}{1-b+c} \\
&\times (1 - \frac{6bc}{1-b+c+4bc} + \frac{2bc}{1-b+c+2bc}) \\
&+ \frac{bc^2}{(1+c)(1-b+c)}(1 + \frac{3bc^2}{(1+c)(1-b+c)-2bc^2} \\
&- \frac{bc^2}{(1+c)(1-b+c)-bc^2})].
\end{aligned}
\tag{19}
$$

Here, $b(\phi(r)) = (9\phi(r)/8)^{1/2}$ and $c(\phi(r)) = 11\phi(r)/16$. To illustrate the implementation of density-dependent diffusion coefficient in our framework, we plot the diffusion-coefficient $D_0(\phi(r))$ (solid line) obtained for the corresponding density distribution $\rho\sigma^3(r)$ (dashed line) obtained using wall-induced lift forces (O) in Fig. 5(a). We note that in our framework, the diffusion-coefficient is lower in regions of high density of hardspheres which is consistent with the observation that diffusion of a hardsphere in regions of high-density can be restricted by caging effects in dense regions [50]. A reduced diffusion-coefficient of the hardspheres in dense regions has implications for the inertial lift forces $F_D^L(r)$ experienced by the hardspheres which is determined from the inertial migration velocity $v_M(r)$ (See eq. 3). Since the hardspheres now diffuse in the radial direction with the density-dependent diffusion coefficient $D_\perp(\phi(r))$ defined in eq. 17, the hardspheres experience a density-dependent lift force $F_D^L(r)$ which is given as:

$$F_D^L(r)/k_BT = v_M(r)/D_\perp(\phi(r)). \tag{20}$$

Hence, a hardsphere in a dense region experiences slow diffusion and consequently an enhanced lift-force $F_D^L(r)$, in comparison to a hardsphere at the same radial position r diffusing with a radial diffusion coefficient $D_\perp$ in a dilute suspension ($\phi = 0$) and experiencing a lift-force $F^L(r)$ given by eq. 3. We note that since the inclusion of density-dependent diffusion coefficient modifies the local inertial lift forces $F_D^L(r)$, the solvent-mediated pair HI inter-
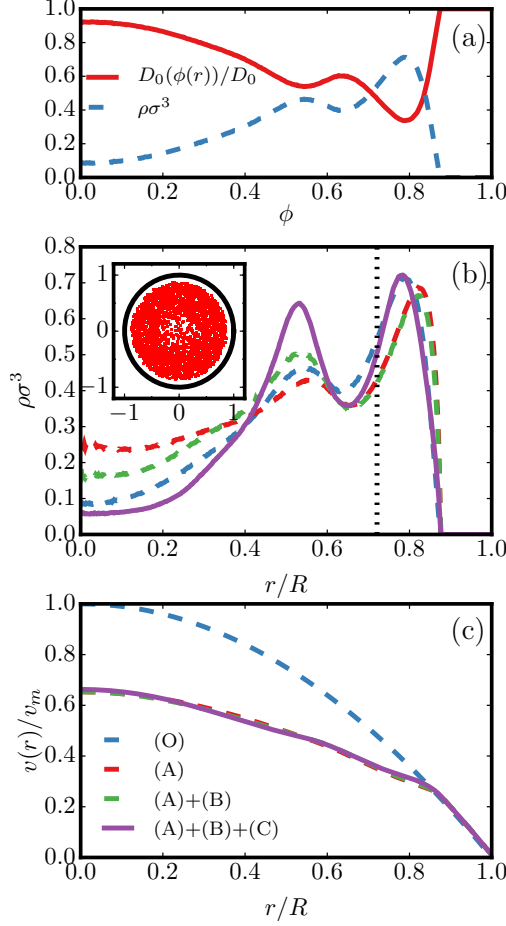
FIG. 5: (a) Density-dependent diffusion-coefficient $D_0(\phi(r))$ and the reduced density $\rho\sigma^3(r)$ plotted along the radial direction (b) Reduced density distribution obtained when the different types of hydrodynamic interactions are included. The density obtained when density-dependent diffusivity is included is indicated by solid line. The legends for plots (b) and (c) are common. The inset shows the five snapshots of positions of the centers of the hardspheres in the radial plane. (c) The velocity distribution obtained for various hydrodynamic interactions.

actions (B) between the hardspheres are also modified since the disturbances caused in the solvent by the hardspheres are now driven by the density-dependent inertial lift forces $F_D^L(r)$.

The reduced density obtained after inclusion of the density-dependent diffusion coefficient $D_\perp(\phi)$ in the simulations is shown by a solid line in Fig. 5(b). The dashed lines represent the density distributions obtained when various HI effects ((O), (O)+(A),(O)+(A)+(B)) are considered as described in earlier sections. Due to the additional density-dependent heterogeneity introduced in the inertial lift forces, we observe increased accumulation of

hardspheres at the positions of the peak of the density distribution which results in the formation of two significant peaks in the reduced density. In addition, we observe an increased depletion of hardspheres in the central region of the cylinder (near $r = 0$) as well as close to the cylindrical wall (near $(R - a)/R$). This is also evident in the inset to Fig. 5(b), in which the position of the centers of hardspheres in the radial plane have been plotted for two snapshots. We can discern a region of low density in the center accompanied by the formation of two concentric rings in which most of the hardspheres are seen to equilibrate. We note that the migration of hardspheres inside the cylinder is driven by the enhanced inertial lift forces $F_D^L(r)$ as well as the collective movement of the hardspheres due to the solvent-mediated hydrodynamic interactions.

Formation of two peaks in the reduced density have been observed in experiments [54, 55] in which the outermost peak corresponds to the position of the Segré-Silberberg annulus. The discussion on the appearance of inner annulus which occurs at high channel Re (Re$\sim 300 - 1400$) in experiments is not conclusive. One experimental study credited the observation of the inner annulus to entrance-length effects [54] and postulated the equilibration of the particles in a single annulus corresponding to the Segré-Silberberg annulus. In a theoretical study, the appearance of the inner annulus has been attributed to a shift in the fixed point of the inertial lift force in a cylindrical pipe to a position closer to the center [56]. In our study, we predict the formation of two peaks at low RePe due to the hydrodynamic interactions inherent in the problem. As RePe is increased for very low volume fractions, the two peaks collapse to a single peak. However, for semi-dilute suspensions, we predict the existence of multiple peaks even at high RePe (Fig. 7).

The change in the local microstructure is reflected in the velocity distribution (see Fig. 5(c)) with a marginal increase in the centerline velocity at $r = 0$ attributed to the enhanced depletion of hardspheres near the wall, accompanied by a marginal decrease in the length of the blunt region. Secondly, we notice the development of oscillations in the velocity distribution similar to those seen in Fig. 4(b), which arise due to the formation of multiple peaks in the reduced density. These effects are expected to be amplified for suspensions flowing with a higher RePe and with a higher density of hardspheres where the hydrodynamic interactions become increasingly significant.

It must be noted that as the inhomogeneity in the radial density increases for semi-dilute suspensions ($\phi > 0.25$) with an increase in RePe, the inhomogeneity in the radial

diffusion-coefficients and the corresponding inertial lift forces increases. In our simulations, the reduced density and the corresponding velocity distribution at this level of inhomogeneity fail to converge. We can overcome this limitation by adopting a smoothed density approximation of the reduced density $\bar{\rho}\sigma^3(r) = \int dr' \rho\sigma^3(r')w(r-r')$ [30], which includes non-local effects of the variation of the density $\rho\sigma^3(r)$ modulated by a weight function $w(r-r')$ to estimate the density-dependent diffusion coefficient at a given radial position r.

Before concluding this section, we would like to summarize the assumptions made in this section. Firstly, we assumed an empirical form of the radial diffusion coefficient $D_\perp(\phi(r))$ which captured effects of the local density based on studies in bulk suspension. Secondly, in this empirical relation, although we considered the effect of confinement on the diffusion coefficient, the effect of the curvature of the cylinder on the diffusion coefficient has not been considered, which gains more importance with increase in confinement. Moreover, given the Cox and Hsu expression for the lift force determined from a single particle moving near a planar wall, the influence of many-body interactions on the lift force felt by a given particle is captured through the modified velocity profile. The variation of the form of $F^L(r)$ itself due to the presence of neighbors is neglected and attributed as an higher order effect.

In the next section, we determine the apparent viscosity of the suspension using the local microstructure and the resulting velocity distribution and discuss the dependence of apparent viscosity of the suspension on the volume fraction, flow velocity, and confinement.

IV. RHEOLOGY OF THE SUSPENSION

As discussed earlier in the introduction, the apparent (effective) viscosity of a colloidal suspension η_{app} is greater than the pure solvent due to the presence of colloids, and is defined as the ratio of the viscosity of the suspension η to the viscosity η_0 of the pure solvent $\eta_{\mathrm{app}} = \eta/\eta_0$. For our suspension of interest, since we can estimate the velocity $v(r)$ of the suspension at radial position r using eq. 6, we can determine the apparent viscosity of the suspension by calculating the flow rate Q of the suspension as:

$$Q = 2\pi \int_0^R rv(r)dr, \quad \eta_{\mathrm{app}} = Q_0/Q, \tag{21}$$

where, Q_0 is the flow rate of the pure solvent. In this section, we investigate the dependence of the apparent viscosity η_{app} on the volume fraction of hardspheres inside the cylinder, the
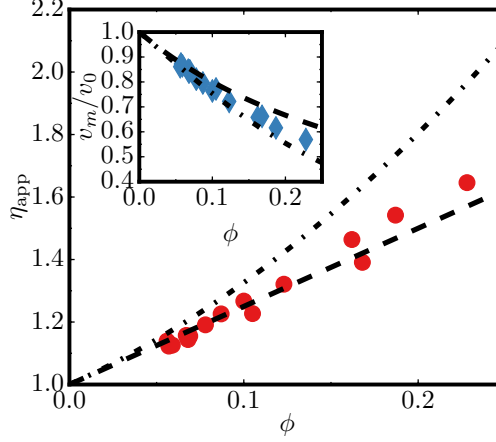
FIG. 6: Apparent viscosity η_{app} plotted as a function of the volume fraction ϕ of the hardspheres in the cylinder. The dashed line indicates the Einstein's prediction of apparent viscosity $\eta_{\text{app}} = 1 + 2.5\phi$ for dilute suspensions and the dashed-dotted line indicates the Batchelor-Green approximation for semi-dilute suspensions $\eta_{\text{app}} = 1 + 2.5\phi + 7.6\phi^2$. The inset shows the variation of the centerline velocity v_m/v_0 with the volume fraction ϕ. The dashed line represents a fit to $1.0/(1 + 2.5\phi)$ and the dashed-dotted line indicates a fit to $1.0/(1 + 2.5\phi + 7.6\phi^2)$.

incoming flow velocity as well as on the confinement effects. We begin with a discussion of the dependence of the apparent viscosity η_{app} on the volume fraction of hardspheres ϕ.

A. Apparent viscosity as a function of ϕ

As discussed in section III, we can equilibrate our suspensions at different volume fractions ϕ using either grand-canonical or canonical simulations in stage I of our simulations. In Table I, we listed the volume fractions ϕ obtained inside the cylinder using grand-canonical simulations for various RePe. These suspensions are then equilibrated with the inclusion of various hydrodynamic interactions (Sec. III B-D) using canonical simulations. After equilibration, we can estimate the apparent viscosity η_{app} of the suspension using eq. 21. We plot the apparent viscosity as a function of the volume fraction in Fig. 6. The dashed line represents Einstein's prediction for dilute suspension $\eta_{\text{E}} = 1 + 2.5\phi$, and the dashed-dotted line represents the Batchelor-Green prediction for semi-dilute suspensions $\eta_{\text{BG}} = 1 + 2.5\phi + 7.6\phi^2$. We note here that these predictions hold for bulk suspensions. We find that the apparent viscosities obtained in our suspensions lie within the bounds of the

27

Einstein's and Batchelor-Green's predictions.

The inset to the figure shows the ratio of the centerline velocity v_m of the suspension to the incident velocity v_0 in the case of a pure solvent for the same pressure difference plotted as a function of volume fraction ϕ of the hardspheres in the confined suspension. The lines represent $1/\eta_{\mathrm{E,BG}}$, where the dashed line is fit to the Einstein's prediction of viscosity η_{E} and the dashed-dotted line represents fit to the Batchelor-Green viscosity η_{BG}. Although experimental results exist for the density distribution of colloids in confined colloidal suspensions undergoing flow which are similar with our predictions [54, 55, 57], there are not sufficient results yet for the centerline velocities of confined suspensions subject to flow in experiments. One experimental attempt for centerline velocities as a function of volume fraction was pursued by Lyon and Leal [38] in rectangular channels in which they predict that the density distribution is peaked at the center. Hence, their predictions of centerline velocities are much higher than is predicted by our model. In the next section, we explore the dependence of apparent viscosity η_{app} on RePe and on confinement effects.

B.   Apparent viscosity as a function of RePe and ratio of diameters D/σ

In this article, we showed that when a hardsphere suspension is subjected to a pressure-driven flow with an incident velocity v_0, the suspension under quasi-equilibrium reorganizes into concentric rings as shown by the peaks in the density distribution (Fig. 3-5). In this section, we explore the change in microstructure with increase in flow velocity or equivalently RePe and study the dependence of apparent viscosity on the local microstructure. In addition, we investigate the dependence of apparent viscosities η_{app} on the confinement of the cylinder i.e. on the ratio of the diameters of the cylinder and the hardspheres D/σ.

We initiate the stage I of our simulation in the canonical ensemble to equilibrate a suspension of hardspheres with volume fraction $\phi = 0.15$ in cylinders of two different diameters such that $D/\sigma = 8, 16$. We vary the flow velocity applied to the suspension such that RePe is varied from $100 - 4000$. The reduced density obtained for the cylinder of diameter $D/\sigma = 8$ at various RePe's is plotted in Fig. 7(a), while the reduced density $\rho\sigma^3$ obtained for suspension in the cylinder of diameter $D/\sigma = 16$ is shown in Fig. 7(b). We observe that the local microstructure of the suspension changes with increasing RePe. As RePe is increased, we first observe that the density of the suspension at the center of the cylinder at $r = 0$ as well
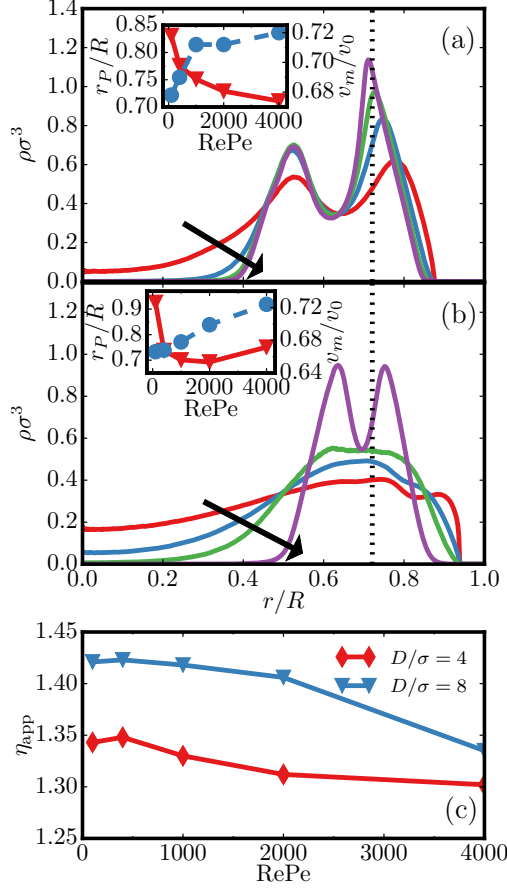
FIG. 7: Reduced density obtained in the canonical ensemble for RePe = 400, 1000, 2000, 4000 (RePe increases along the direction of the arrow). Volume fraction of hardspheres in the cylinder is $\phi = 0.15$. The diameter of the cylinder is $D/\sigma = 8$ and 16 for (a) and (b) respectively. The inset to the figures show the variation of the position r_P/R of the primary peak (left axis, solid line) and v_m/v_0 (right axis, dashed line) as a function of RePe. (c) The apparent viscosity η_{app} of the suspension with volume fraction $\phi = 0.15$ plotted as a function of RePe for two diameters of the cylinder $D/\sigma = 8, 16$.

as near the cylindrical wall (at $r = R - \sigma$) decreases. Secondly, the hardspheres accumulate close to r_C. This is also evident in the insets to Figs. 7(a),(b), in which the position of the primary peak r_P in the reduced density is plotted as a function of RePe. We see that r_P approaches r_C as RePe is increased.

This change in the local microstructure has implications for the velocity of the suspension as well as for the apparent viscosity of the suspension. We plot the normalized centerline velocity of the suspension v_m/v_0 obtained for various RePe's in the inset to Figs. 7(a),(b).

29

we observe that the normalized centerline velocity v_m/v_0 increases as RePe increases. This is a direct effect of the change in the microstructure of the suspension. Since the density of particles near the wall decreases and shifts to the central regions as RePe is increased, an increasing number of hardspheres are moving with a faster velocity, thereby increasing the flow rate Q of the suspension. As a result, as is shown in Fig. 7(c), the apparent viscosity of the suspension for the two diameters decreases as RePe is increased. This is indicative of a shear-thinning behavior, and has been observed in bulk hardsphere suspensions [58]. However, there have been limited experiments that have measured apparent viscosities in confined geometries. Furthermore, the apparent viscosity is higher for the suspension in the cylinder with the larger diameter. In the case of complex fluids such as suspension of red blood cells [59], it has been observed that the viscosities increase with increase in diameter of the channel/pipe. Hence, our simulations capture the salient changes in the viscosity of confined suspensions with variation in flow rate, tube diameter and volume fraction.

V. CONCLUSIONS

To conclude, we studied the microstructure and rheology of a hardsphere suspension confined in a cylindrical channel and driven by a pressure-driven flow using MC simulations. To include the various hydrodynamic interactions active in the system, we developed particle-based MC simulations which includes interactions due to wall-induced inertial forces acting on the hardspheres, solvent-mediated HI between the hardspheres, and density-dependent diffusivity, from which we have estimated the velocity and density of the suspension in the radial direction using a self-consistent calculation. We showed that the hydrodynamic interactions gives rise to enhanced peaks in the confined suspension in flow, and leads to enhanced depletion of hardspheres near the wall. As a result, the apparent viscosity increases with increasing hardsphere volume fraction, decreases with increasing flow velocity, and increases for cylindrical channels with larger diameters. In future outlook, this study can be extended for particles with more complicated geometries such as anisotropic particles [4], soft particles which can interact with each other using Lennard-Jones potential, and to complicated geometries of the confinement.

Acknowledgments

---

[1] R. Fahraeus and T. Lindqvist, Am. J. Physiol. **96**, 562 (1931).

[2] T. M. Geislinger and T. Franke, Advances in Colloid and Interface Science **208**, 161 (2014).

[3] D. J. Jeffrey and A. Acrivos, AIChE Journal **22**, 417 (1976).

[4] S. Mueller, E. W. Llewellin, and H. M. Mader, **466**, 1201 (2010).

[5] A. Einstein, Ann. Phys. **34**, 591 (1911).

[6] G. K. Batchelor and J. T. Green, Journal of Fluid Mechanics **56**, 401 (1972).

[7] I. M. Krieger and T. J. Dougherty, Transactions of the Society of Rheology **3**, 137 (1959).

[8] J. S. Chong, E. B. Christiansen, and A. D. Baer, Journal of Applied Polymer Science **15**, 2007 (1971).

[9] C. G. de Kruif, E. M. F. van Iersel, A. Vrij, and W. B. Russel, The Journal of Chemical Physics **83**, 4717 (1985).

[10] K. Nygård, S. Sarman, K. Hyltegren, S. Chodankar, E. Perret, J. Buitenhuis, J. F. van der Veen, and R. Kjellander, Phys. Rev. X **6**, 011014 (2016).

[11] J. Mittal, T. M. Truskett, J. R. Errington, and G. Hummer, Phys. Rev. Lett. **100**, 145901 (2008).

[12] W. Fornari, L. Brandt, P. Chaudhuri, C. U. Lopez, D. Mitra, and F. Picano, Phys. Rev. Lett. **116**, 018301 (2016).

[13] K. Yeo and M. R. Maxey, Phys. Rev. E **81**, 051502 (2010).

[14] B. H. Yang, J. Wang, D. D. Joseph, H. H. Hu, T.-W. Pan, and R. Glowinski, Journal of Fluid Mechanics **540**, 109 (2005).

[15] A. J. Ladd, Molecular Physics **113**, 2531 (2015).

[16] P. R. Nott and J. F. Brady, Journal of Fluid Mechanics **275**, 157 (1994).

[17] U. M. B. Marconi and P. Tarazona, J. Chem. Phys. **110**, 8032 (1999).

[18] A. J. Archer and R. Evans, J. Chem. Phys. **121**, 4246 (2004).

[19] M. Schmidt and J. M. Brader, J. Chem. Phys. **138**, 214101 (2013).

[20] B. D. Goddard, A. Nold, and S. Kalliadasis, J. Chem. Phys. **145**, 214106 (2016).

[21] D. Henderson, ed., <u>Fundamentals of Inhomogeneous Fluids</u> (Marcel Dekker, New York, 1992).

[22] J. M. Brader and M. Krüger, Mol. Phys. **109**, 1029 (2011).

[23] A. Scacchi, M. Krüger, and J. M. Brader, J. Phys.: Condens. Matter **28**, 244023 (2016).

[24] M. Rex and H. Löwen, Phys. Rev. Lett. **101**, 148302 (2008).

[25] M. Rex and H. Löwen, Eur. Phys. J. E **28**, 139âĂŞ146 (2009).

[26] L. Almenar and M. Rauscher, Journal of Physics: Condensed Matter **23**, 184115 (2011).

[27] M. Grmela, G. Maîtrejean, F. Chinesta, and A. Ammar, Rheologica Acta **52**, 557 (2013).

[28] C. P. Royall, J. Dzubiella, M. Schmidt, and A. von Blaaderen, Phys. Rev. Lett. **98**, 188304 (2007).

[29] H.-Y. Yu, Z. Jabeen, D. M. Eckmann, P. S. Ayyaswamy, and R. Radhakrishnan, Langmuir **33**, 11332 (2017).

[30] P. Tarazona, Phys. Rev. A **31**, 2672 (1985).

[31] N. F. Carnahan and K. E. Starling, J. Chem. Phys. **51** (1969).

[32] G. Segré and A. Silberberg, J. Fluid Mech **14**, 136 (1962).

[33] D. Frenkel and B. Smit, <u>Understanding Molecular Simulation: From Algorithms to Applications</u> (Academic Press, 2001), 2nd ed., ISBN 9780122673511.

[34] D. Bratko, L. Blum, and M. S. Wertheim, The Journal of Chemical Physics **90** (1989).

[35] R. G. Cox and S. K. Hsu, Int. J. Multiph. Flow **3**, 201 (1977).

[36] M. A. Bevan and D. C. Prieve, The Journal of Chemical Physics **113**, 1228 (2000).

[37] R. E. Hampton, A. A. Mammoli, A. L. Graham, , N. Tetlow, and S. A. Altobelli, J. Rheol. **41**, 621 (1997).

[38] M. K. Lyon and L. G. Leal, J. Fluid Mech. **363**, 25 (1998).

[39] B. P. Ho and L. G. Leal, J. Fluid Mech. **65**, 365 (1974).

[40] K. P. Travis, B. Todd, and D. J. Evans, Physica A: Statistical Mechanics and its Applications **240**, 315 (1997).

[41] P. J. Zuk, E. Wajnryb, K. A. Mizerski, and P. Szymczak, Journal of Fluid Mechanics **741**, R5 (2014).

[42] E. Wajnryb, K. A. Mizerski, P. J. Zuk, and P. Szymczak, Journal of Fluid Mechanics **731**, R3 (2013).

[43] J. F. Brady and G. Bossis, Annual Review of Fluid Mechanics **20**, 111 (1988).

[44] J. Rotne and S. Prager, The Journal of Chemical Physics **50**, 4831 (1969).

[45] H. Yamakawa, The Journal of Chemical Physics **53**, 436 (1970).

[46] J. R. Blake, Mathematical Proceedings of the Cambridge Philosophical Society **70**, 303 (1971).

[47] M. Rex and H. Löwen, Phys. Rev. Lett. **101**, 148302 (2008).

[48] A. Sierou and J. F. Brady, Journal of Fluid Mechanics **448**, 115 (2001).

[49] M. Tokuyama and I. Oppenheim, Physica A: Statistical Mechanics and its Applications **216**, 85 (1995).

[50] R. Verberg, I. M. de Schepper, and E. G. D. Cohen, Phys. Rev. E **61**, 2967 (2000).

[51] A. J. C. Ladd, H. Gang, J. X. Zhu, and D. A. Weitz, Phys. Rev. E **52**, 6550 (1995).

[52] S. Ghosh, D. Wijnperle, F. Mugele, and M. H. G. Duits, Soft Matter **12**, 1621 (2016).

[53] H. B. Eral, J. M. Oh, D. van den Ende, F. Mugele, and M. H. G. Duits, Langmuir **26**, 16722 (2010).

[54] Y. Morita, T. Itano, and M. Sugihara-Seki, Journal of Fluid Mechanics **813**, 750 (2017).

[55] J.-P. Matas, J. Morris, and E. Guazzeli, J. Fluid. Mech. **515**, 171 (2004).

[56] J.-P. Matas, J. F. Morris, and E. Guazzelli, Journal of Fluid Mechanics **621**, 59 (2009).

[57] Y.-S. Choi and S.-J. Lee, Microfluidics and Nanofluidics **9**, 819 (2010).

[58] R. G. Larson, <u>The Structure and Rheology of Complex Fluids</u> (Oxford University Press, 1998), 1st ed., ISBN 978-0195121971.

[59] A. R. Pries, D. Neuhaus, and P. Gaehtgens, American Journal of Physiology-Heart and Circulatory Physiology **263**, H1770 (1992).